Effects of geometrical nonlinearities for a rotating intentionally mistuned bladed-disk

Anthony Picou, Evangéline Capiez-Lernout, Christian Soize, Moustapha Mbaye

Effects of geometrical nonlinearities for a rotating intentionally mistuned bladed-disk.

A. Picou [1,2], **E. Capiez-Lernout** [1], **C. Soize** [1], **M. Mbaye** [2]
[1] Université Paris-Est, Laboratoire Modélisation et Simulation Multi-Echelle, MSME UMR 8208 CNRS, 5 bd Descartes, 77454 Marne-La-Vallée Cedex 02, France
[2] Safran Tech - Safran Group, 78114 Magny-Les-Hameaux, France
e-mail: **anthony.picou@u-pem.fr**

Abstract
The present paper describes a computational methodology adapted to the analysis of the nonlinear dynamical behavior of a detuned bladed disk. The context of the analysis is the following : (1) the detuning is taken into account by voluntarily breaking the cyclic symmetry of the structure with the use of a pattern constituted of different blade types; (2) the structure is assumed to undergo large strain/displacements induced by the geometrical nonlinear effects; (3) the prestresses and the gyroscopic effects induced by the rotating motion are considered in the nonlinear dynamical analysis. The computational strategy has to be compatible with the industrial context. Consequently, a particular attention is paid to the construction of an adapted nonlinear reduced-order model. Finally, the proposed methodology is applied on a complex bladed disk structure.

1 Introduction

In turbomachinery, the mistuning of bladed-disks structures caused by the manufacturing tolerances and the small variations in the mechanical properties from blade to blade is known to amplify and to localize the dynamical response of some blades [1, 2]. There have been various researches concerning the computational modeling of mistuned structures, with the development of reduced-order models (see for instance [3, 4, 5] for linear reduced-order models and [6, 7] for nonlinear reduced-order models) and probabilistic approaches [8, 9]. One possible strategy is also to intentionally mistune (detuning) the structure by assembling generating sectors of different types according to a given pattern [10, 11, 12]. The pattern optimization is known to be efficient for reducing the response amplitudes in the linear context. Nevertheless, geometrical nonlinear effects can no longer be neglected with the current technological improvements, including the use of more flexible and lighter materials which sometimes leads to large displacements and strains. In this context, the present research is devoted to the computational analysis of geometrical nonlinear effects on a rotating detuned bladed disk. The research is focused on a computational strategy for which a nonlinear reduced-order model compatible with the consideration of both mistuning and detuning phenomena is introduced. In the present context, we limit the investigation only to the case of detuning. The paper is organized as follows. The first Section is devoted to the development of the methodology. In particular, an adapted nonlinear reduced-order basis is constructed for the detuned structure with a double projection method. Such method involves a first projection of the nonlinear dynamical response on the usual eigenmodes of vibrations followed by a Proper Orthogonal Decomposition of the related nonlinear response including the gyroscopic coupling effects. In a second Section, a numerical application concerning a realistic computational model of bladed-disk is considered. The nonlinear responses of the tuned rotating structure and of a detuned rotating structure corresponding to a given pattern are analyzed.

2 Methodology

In this Section, a methodology adapted to the nonlinear dynamical analysis of a rotating detuned bladed-disk is developed. In this context of detuning, it is assumed that the bladed-disk is constituted of N sectors that can be different from one sector to another one. A detuned bladed disk is constructed according to a given pattern $\mathcal{P}$ which defines the distribution of the different sectors that constitute the detuned bladed-disk structure. Furthermore, the constitutive equations are assumed to be linear elastic but the external loads are assumed to be sufficiently large so that the structure undergoes geometrical nonlinear effects induced by the large displacements and strains.

2.1 Nonlinear finite element model of the detuned bladed-disk

The computational model is constructed by using three-dimensional isoparametric solid finite elements. Let P be the number of available sectors whose mesh is assumed to be compatible at the interface of each sector. The full bladed-disk is constructed by the assembly of each sector type according to a given pattern $\mathcal{P}$. Let n be the number of dofs of the finite element mesh. The nonlinear finite element computational model that describes the nonlinear dynamical behavior of the detuned structure at a given rotational velocity Ω consists in finding the $\mathbb{R}^n$-vector $\mathbf{U}$ of the displacements, solution of the following nonlinear differential equation

$$[M]\ddot{\mathbf{U}}(t) + \Big([D] + [C_g(\Omega)]\Big)\dot{\mathbf{U}}(t) + \Big([K_e] + [K_c(\Omega)] + [K_g(\Omega)]\Big)\mathbf{U}(t) + \mathbf{F}^{\mathrm{NL}}(\mathbf{U}(t)) = \mathbf{F}(t)\,, \qquad (1)$$

in which the $(n \times n)$ real matrices $[M]$, $[D]$, $[C_g(\Omega)]$, $[K_e]$, $[K_c(\Omega)]$ and $[K_g(\Omega)]$ are respectively the mass matrix with symmetry and positive definiteness properties, the damping matrix with symmetry and positive semi-definiteness properties, the gyroscopic coupling matrix with antisymmetry property, the elastic stiffness matrix with symmetry and positive definiteness properties, the centrifugal stiffness matrix with symmetry and negative definiteness properties, and the geometrical stiffness matrix with symmetry and positive definiteness properties. Matrix $[K_g(\Omega)]$ is beforehand constructed using the stress state issued from a linear static analysis for which each type of sector is subjected to a centrifugal load [13]. It is assumed that the finite element matrix $[K_e] + [K_c(\Omega)] + [K_g(\Omega)]$ remains symmetric positive-definite for the considered valued of Ω. In equation (1), the $\mathbb{R}^n$-vector $\mathbf{F}(t)$ is issued from the discretization of the external loads and the $\mathbb{R}^n$-vector $\mathbf{F}^{\mathrm{NL}}(\mathbf{U}(t))$ describes the nonlinear finite element internal forces induced by the geometrical nonlinearities. In the present strategy, we are interested in analyzing the nonlinear forced response in the time domain. In consequence, the external load is defined for $t \in \mathbb{R}$. A Fourier transform performed on the solution of Eq.(1) allows then the nonlinear dynamical response in the frequency domain to be analyzed.

2.2 Nonlinear reduced-order model for a detuned bladed-disk

In this Section, the method used for constructing the nonlinear reduced-order model of the detuned bladed-disk is presented. The main idea is to use a double projection method. A first projection basis is constructed by solving the generalized eigenvalue problem related to the conservative and homogeneous dynamical equation for which the gyroscopic coupling is ignored. In a second step, this projection basis is used for constructing the nonlinear reduced-order model related to Eq.(1) (that includes the gyroscopic coupling effects). A new projection basis is then computed from this nonlinear reduced-order response with the Proper Orthogonal Decomposition method [14].

2.2.1 Construction of the first projection basis

First, let us consider the following generalized eigenvalue problem

$$\Big([K_e] + [K_c(\Omega)] + [K_g(\Omega)]\Big)\,\boldsymbol{\varphi_\alpha} = \lambda_\alpha\,[M]\,\boldsymbol{\varphi_\alpha}\,. \qquad (2)$$

Note that such projection basis does not correspond to the homogeneous conservative equation since the gyroscopic coupling term is ignored in the definition of the present generalized eigenvalue problem (if the gyroscopic coupling was taken into account, a nonsymmetric complex eigenvalue problem should be solved). In (2), the eigenvalues λ_α, $\alpha = \{1, ..., n\}$ related to the elastic modes $\boldsymbol{\varphi_\alpha}$ are sorted by increasing order $0 < \lambda_1 \leqslant \lambda_2 \leqslant \cdots \leqslant \lambda_n$. The $m \lll n$ eigenvectors related to the first m eigenvalues are computed. Let $[\Phi]$ be the $(n \times m)$ real modal matrix defined by

$$[\Phi] = [\boldsymbol{\varphi_1} \ldots \boldsymbol{\varphi_m}] \,. \tag{3}$$

2.2.2 Construction of the second projection basis

The second projection basis is obtained by considering the first nonlinear reduced-order model that is constructed by projection of Eq. (1) on the subspace spanned by $\{\boldsymbol{\varphi_1}, \ldots, \boldsymbol{\varphi_m}\}$,

$$\mathbf{U}(t) = [\Phi]\, \mathbf{Q}_0(t) \quad , \tag{4}$$

$$[\mathcal{M}_0]\ddot{\mathbf{Q}}_0(t) + \Big([\mathcal{D}_0] + [\mathcal{C}_0(\Omega)] \Big) \dot{\mathbf{Q}}_0(t) + [\mathcal{K}_0(\Omega)]\mathbf{Q}_0(t) + \boldsymbol{\mathcal{F}}^{NL}(\mathbf{Q}_0(t)) = \boldsymbol{\mathcal{F}}_0(t) \,, \tag{5}$$

in which the $\mathbb{R}^m$-vector $\mathbf{Q}_0(t) = (Q_1(t), \cdots, Q_m(t))$ is the vector of the generalized coordinates and where the generalized mass, damping, gyroscopic coupling, and stiffness matrices $[\mathcal{M}_0]$, $[\mathcal{D}_0]$, $[\mathcal{C}_0(\Omega)]$, and $[\mathcal{K}_0(\Omega)]$ are defined by

$$\begin{aligned} [\mathcal{M}_0] &= [\Phi]^T[M][\Phi] \quad , \quad [\mathcal{D}_0] = [\Phi]^T[D][\Phi] \quad , \quad [\mathcal{C}_0(\Omega)] = [\Phi]^T[C_g(\Omega)][\Phi] \\ [\mathcal{K}_0] &= [\Phi]^T \Big([K_e] + [K_g(\Omega)] + [K_c(\Omega)] \Big) [\Phi] \end{aligned} \tag{6}$$

In Eq. (5), the $\mathbb{R}^m$-vectors of the reduced external load and of the nonlinear reduced internal load are written as

$$\boldsymbol{\mathcal{F}}_0(t) = [\Phi]^T \mathbf{F}(t) \quad , \quad \boldsymbol{\mathcal{F}}^{NL}(\mathbf{Q}_0(t)) = [\Phi]^T \mathbf{F}^{\mathrm{NL}}([\Phi]\, \mathbf{Q}_0(t)) \,. \tag{7}$$

In the present context, the reduced nonlinear stiffness operators are first explicitly constructed with the finite element method from the knowledge of the projection basis [15] and the nonlinear reduced internal loads are computed from these nonlinear reduced operators. Note that such strategy is compatible with the possibility of implementing random uncertainties [16], which is not considered in the present work. The nonlinear differential equation (5) is solved in the time domain and the corresponding solution $\mathbf{Q}_0(t)$ is then used for constructing a new reduced-order basis with the POD method. Let n_t be the number of time steps and let $\{t_j, j = 1, \ldots, n_t\}$ be the sampling time points. We then introduce the $(m \times n_t)$ real matrix $[Y]$ and the $(m \times m)$ real correlation matrix $[A]$ such that

$$[Y]_{ij} = Q_{0,i}(t_j) \sqrt{t_j - t_{j-1}} \quad , \quad [A] = [Y]\,[Y]^T \,. \tag{8}$$

The projection basis is then defined as the eigenvectors $\mathcal{W}_1, \cdots, \mathcal{W}_p$ of the correlation matrix $[A]$ related to the p most contributing eigenvalues $\mu_1 \geq \cdots \geq \mu_p$ such that

$$[A]\, \mathcal{W}_\alpha = \mu_\alpha\, \mathcal{W}_\alpha \,. \tag{9}$$

Let $[\mathcal{W}]$ be the $(m \times p)$ matrix whose columns are these p eigenvectors. The new projection basis that will be used for solving the nonlinear dynamical problem is characterized by the $(n \times p)$ matrix $[\Psi]$ such that

$$[\Psi] = [\Phi][\mathcal{W}] \,. \tag{10}$$

The nonlinear reduced-order model is then obtained by projecting the solution $\mathbf{U}$ of the nonlinear finite element equation such that

$$\mathbf{U}(t) = [\Psi]\mathbf{Q}(t) \quad , \tag{11}$$

in which $\mathbf{Q}(t)$ is the $\mathbb{R}^p$-vector of the generalized coordinates solution of the nonlinear differential equation

$$[\mathcal{M}]\ddot{\mathbf{Q}}(t) + \Big([\mathcal{D}] + [\mathcal{C}(\Omega)]\Big)\dot{\mathbf{Q}}(t) + [\mathcal{K}]\mathbf{Q}(t) + \boldsymbol{\mathcal{F}}^{\mathrm{NL}}(\mathbf{Q}(t)) = \boldsymbol{\mathcal{F}}(t)\,, \tag{12}$$

in which the generalized mass, damping, gyroscopic coupling, and stiffness matrices $[\mathcal{M}]$, $[\mathcal{D}]$, $[\mathcal{C}(\Omega)]$, $[\mathcal{K}(\Omega)]$, the reduced external load vector $\boldsymbol{\mathcal{F}}(t)$ and the nonlinear reduced internal load vector $\boldsymbol{\mathcal{F}}^{\mathrm{NL}}(\mathbf{Q}(t))$ are defined similarly to (7).

This nonlinear reduced-order model can be useful for two main reasons. For instance, let us consider all the patterns related to a given number of sectors for each sector type. This leads us to parameterize the nonlinear reduced-order model with respect to a given parameter μ for which n_μ is the number of possible different patterns. At this point, the calculation of the reduced-order basis $[\Psi(\mu)]$ can be carried out for $m_\mu < n_\mu$ judicious values of μ following for instance greedy strategies. Such parameterized reduced-order basis is then wisely merged for constructing an optimal global reduced-order basis $[\Psi]$, which is use for solving any pattern of interest. Otherwise, let us consider the case for which both detuning and mistuning phenomena are investigated for a given pattern. In such case, if the mistuning is implemented through the nonparametric probabilistic approach, an optimal reduced-order basis is required in order to solve the related stochastic nonlinear differential equations.

3 Numerical application

In this section, a numerical application concerning the nonlinear dynamical analysis of a bladed-disk structure is investigated in the detuning context.

3.1 Description of the finite element computational model

The geometric features of the generating sector are summarized in Table 1. Such given reference sector will be called the sector of type 1. The computational model of this reference sector and issued from the finite element method is provided with the commercial software ANSYS. This computational model is then used for constructing the computational model of the whole tuned bladed-disk with $N = 24$ blades, which will be taken as a reference. The structure is made of steel, and is assumed to be homogeneous and isotropic with Young modulus $E = 2 \times 10^{11}\, N \times m^{-2}$, Poisson ratio $\nu = 0.3$, and mass density $\rho = 7\,650\, Kg \times m^{-3}$. The structure is clamped at the inner radius of the disk sector. The numerical finite element mesh is constituted of tridimensional solid finite elements with 20 nodes (bricks element), tridimensional solid finite elements with 13 nodes (pyramidal elements) and tridimensional solid finite elements with 10 nodes (tetrahedral elements), corresponding to a quadratic interpolation. The numerical data related to the finite element model are summarized in Table 2. Figure 1 displays the 3D finite element mesh of the bladed-disk structure.

Inner disk Radius	19.8 mm
Outer disk Radius	100 mm
Disk width	20 mm
Blade thickness at root section	4.8 mm
Blade thickness at tip section	2 mm

Table 1: Geometric parameters of the generating sector

The detuned bladed-disk structure is then considered by defining another generating sector, which is obtained by decreasing the Young modulus E of the blade of the type-1 generating sector by $25\,\%$. Consequently, there is type-1 generating sector with Young modulus $E = 2 \times 10^{11}\, N \times m^{-2}$ for the blade and a type-2

Structure	Elements	Nodes	DOFs
Blade sector	2,714	6,896	20,688
Disk sector	836	4,554	13,662
Full structure	85,200	265,080	787,176

Table 2: Numerical finite element parameters for the generating sector and for the full structure

generating sector with Young modulus $E = 1.5 \times 10^{11}\, N \times m^{-2}$ for the blade, the Young modulus of the disk remaining to $E = 2 \times 10^{11}\, N \times m^{-2}$. In the following, it is assumed that there are 2 blades of type 2 and 22 blades of type 1, which defines many possible patterns. The assembly of the full detuned bladed-disk computational model is then performed according to a given pattern.

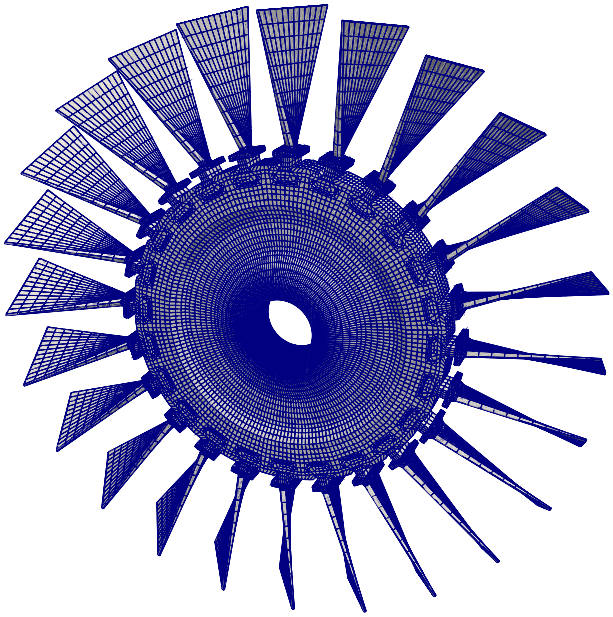

Figure 1: Finite element model of the bladed-disk.

The analysis is performed for two patterns. A cyclic pattern denoted as $\mathcal{P}_1$ that is defined by

$$\mathcal{P}_1 \;=\; [1\,1\,1\,1\,1\,1\,1\,1\,1\,1\,1\,1\,1\,1\,1\,1\,1\,1\,1\,1\,1\,1\,1\,1]\,, \tag{13}$$

and we consider a detuned pattern denoted by $\mathcal{P}_2$ and represented in Fig.2 such that

$$\mathcal{P}_2 \;=\; [1\,1\,1\,1\,1\,1\,1\,1\,1\,2\,1\,1\,1\,2\,1\,1\,1\,1\,1\,1\,1\,1\,1\,1] \quad . \tag{14}$$

3.2 Choice of the excitation force

Figure 3 represents the graph of the eigenfrequencies $\nu_\alpha = \sqrt{\lambda_\alpha}$, solution of Eq. (2) related to the tuned structure defined by $\mathcal{P}_1$ with a rotating velocity $\Omega = 465\, rad \times s^{-1}$ with respect to its circumferential wave number h.

This graph allows the excitation frequency band favorable to drastic mistuning effects to be defined. In the present case, a $h = 4$ engine-order excitation is chosen because there are two close eigenfrequencies issued from two different class of vibrational modes. In consequence, the time repartition of the load $g(t)$

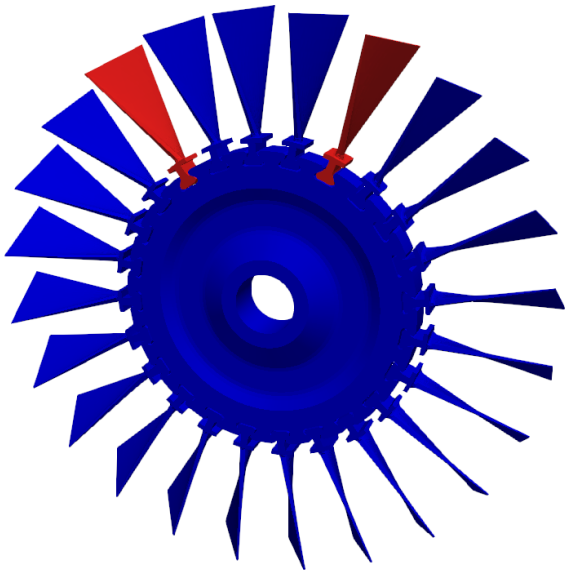

Figure 2: Pattern $\mathcal{P}_2$ for the detuned bladed-disk

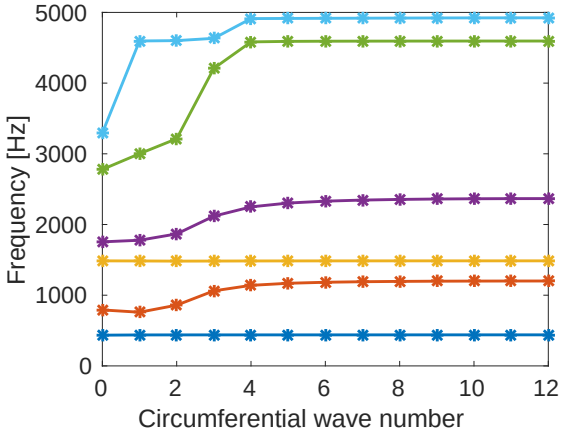

Figure 3: Graph $h \mapsto \nu_\alpha(h)$ of the eigenfrequencies ν_α related to the tuned pattern $\mathcal{P}_1$ of the rotating bladed-disk with respect to its corresponding circumferential wavenumber h.

is constructed so that an excitation frequency band $\mathbb{B}_e = [1000, 1600]\, Hz$ is uniformly excited. Let $\nu_{min} = 1\,000\, Hz$ and $\nu_{max} = 1\,600\, Hz$. We then have

$$g(t) = \sum_{i=1}^{Q} \frac{2}{\pi\, t} \sin(\pi\, \delta\nu\, t)\, \cos(2\pi s_i\, \delta\nu\, t)\,, \tag{15}$$

in which Q is chosen such that $Q = 10$. In Eq.(15), we have

$$\delta\nu = \frac{\nu_{max} - \nu_{min}}{Q} \quad , \quad s_i = \frac{\nu_{min}}{\delta\nu} + \left(i - \frac{1}{2}\right)\,. \tag{16}$$

As a consequence, the Fourier transform of function $g(t)$ is such that $|\hat{g}(2\pi\nu)| = 1$ on $\mathbb{B}_e$. Note that function $g(t)$ is theoretically defined for $t \in \mathbb{R}$ in order to consider in the time domain the problem of forced response. In the numerical process, the signal is truncated by choosing $t_{ini} = -0.065\, s$ such that $g(t_{ini}) = 0$ with a time duration $T = 0.35\, s$, ensuring the low frequencies located outside $\mathbb{B}_e$ to possibly be captured when

considering geometric nonlinear calculations. The sample frequency and the number of time steps are chosen as $\nu_e = 10\,000\,Hz$ and $n_t = 4\,096$ yielding a frequency resolution $\delta\nu_0 = 2.44\,Hz$. The dynamical analysis is carried out in the frequency band of analysis $\mathbb{B} = [0\,,\,4\,000]Hz$. Figure 4 shows the graph of the time repartition of the load $t \to g(t)$ and its Fourier transform $\nu \to |\widehat{g}(2\pi\nu)|$. The spatial repartition of the external load is a normalized vector $\mathbb{F}$ for which all directions related to the node located at the tip of each blade are simultaneously excited. The load intensity f_0 is given by $f_0 = 1.2\,N$ for which it will be shown below that geometrical nonlinear effects can be observed. The load vector $\mathbf{F}(t)$ is then defined in the time domain by

$$\mathbf{F}(t) = s_0\, g(t)\, \mathbb{F} \quad . \tag{17}$$

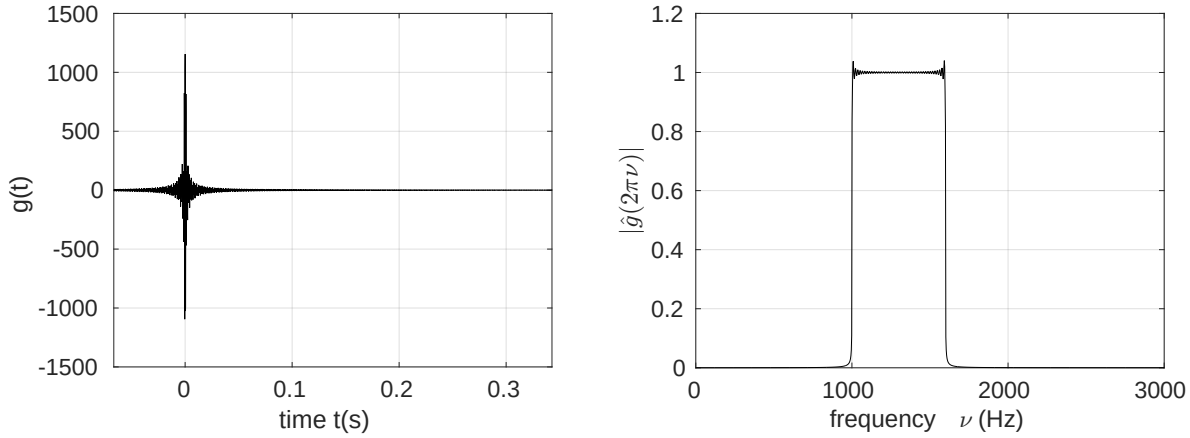

Figure 4: Representation of the external load in the time domain and in the frequency domain: graph of $t \mapsto g(t)$ (left graph) and $\nu \mapsto |\widehat{g}(2\pi\nu)|$ (right graph) for $\mathbb{B}_e = [1000\,,\,1600]\,Hz$.

3.3 Convergence analysis

Let $n_{obs} = N$ be the number of observation points located at the tip of each blade of the detuned bladed-disk. Let $\mathbf{U}_i^{obs,j}(t)$, with $j = 1, \ldots, n_{obs}$ and $i = 1, 2, 3$, be the displacement at observation node j according to dof i and let $\widehat{\mathbf{U}}_i^{obs,j}(2\pi\nu)$ be its Fourier Transform. We then define the scalar quantity W^{obs} such that

$$\widehat{W}^{obs}(2\pi\nu) = \sqrt{\sum_{j=1}^{n_{obs}} ||\hat{\mathbf{U}}^{obs,j}(2\pi\nu)||^2} \quad , \quad ||\hat{\mathbf{U}}^{obs,j}(2\pi\nu)||^2 = \sum_{i=1}^{3} |\hat{\mathbf{U}}_i^{obs,j}(2\pi\nu)|^2 \,. \tag{18}$$

Let $\widehat{W}_{LIN}^{obs,(m,p)}(2\pi\nu)$ or $\widehat{W}_{NONLIN}^{obs,(m,p)}(2\pi\nu)$ be the observation computed with the linear or with the nonlinear reduced-order model obtained with the first reduction, $p = m$, or with the second reduction, $p < m$. Subscript LIN and $NONLIN$ are omitted as soon as there is no possible confusion. A first convergence analysis is performed with respect to the number m of modes kept in the first reduced-order model. Let $Conv_1(m)$ be the function defined by

$$Conv_1(m) = \sqrt{\int_{\mathbb{B}} \left(\widehat{W}^{obs,(m,m)}(2\pi\nu)\right)^2 d\nu} \quad , \tag{19}$$

for which observation $\widehat{W}^{obs,(m,m)}(2\pi\nu)$ is constructed by solving Eq. (5). Figure 5 displays the graphs of functions $m \mapsto Conv_{1,LIN}(m)$ and $m \mapsto Conv_{1,NONLIN}(m)$. It can be seen that a good approximation is obtained for $m = 60$ for the linear case and for $m = 100$ for the nonlinear case. In the following, all the computations are carried out with $m = 100$.

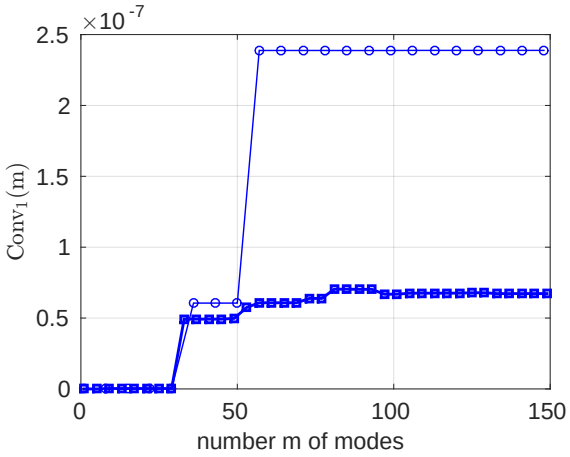

Figure 5: Convergence analysis related to the first reduced-order model: graphs of $m \mapsto Conv_{1,LIN}(m)$ related to the first linear reduced-order model (thin line, $\circ$ marker) and of $m \mapsto Conv_{1,NONLIN}(m)$ related to the first reduction (thick line, $\square$ marker).

For fixed m, a second convergence analysis is then carried out with respect to the number p of basis vectors calculated with Eqs. (9) and (10). Let $Conv_2(m,p)$ be the function defined by

$$Conv_2(m,p) = \sqrt{\int_{\mathbb{B}} \left(\widehat{W}^{obs,(m,p)}(2\pi\nu) \right)^2 d\nu} \quad , \tag{20}$$

for which observation $\widehat{W}^{obs,(m,p)}(2\pi\nu)$ is constructed by solving Eq. (12). Figure 6 displays the graph of functions $m \mapsto Conv_{2,NONLIN}(m = 100, p)$. It can be seen that a good approximation is obtained for $m = 100$ and $p = 20$, which proves the efficiency of this proposed second reduction method.

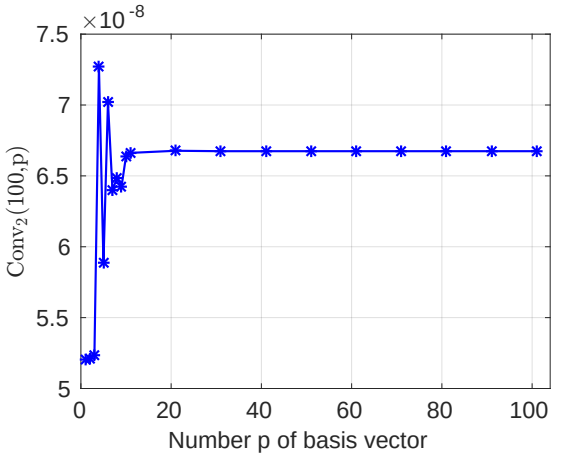

Figure 6: Convergence analysis related to the second nonlinear reduced-order model : graphs of $p \mapsto Conv_{2,NONLIN}(m,p)$ related to the second reduction (thick line, $\star$ marker).

3.4 Load sensitivity analysis

In this section, a load sensitivity is performed for pattern $\mathcal{P}_1$ in order to determine from which load intensity f_0, there are geometrical nonlinear effects in the dynamical response of the structure. Such analysis is performed by quantifying the energy outside the excitation frequency band $\mathbb{B}_e$ for f_0 belonging to $[0\,,\,1.9]\,N$.

We then define by $Conv_F(f_0)$ the quantity written as

$$Conv_F(f_0) = \frac{\sqrt{\int_{\mathbb{B}\setminus\mathbb{B}_e} \left(\widehat{W}^{obs,(m,m)}_{NONLIN}(2\pi\nu; f_0)\right)^2 d\nu}}{\sqrt{\int_{\mathbb{B}\setminus\mathbb{B}_e} \left(\widehat{W}^{obs,(m,m)}_{NONLIN}(2\pi\nu; 1.9)\right)^2 d\nu}} \quad . \tag{21}$$

Figure 7 displays the graph of $f_0 \mapsto Conv_F(f_0)$. It can be seen that geometrical nonlinear effects can be seen for $f_0 > 0.3\,N$. Figure 8 displays the graphs of $\nu \mapsto ||\widehat{\mathbf{U}}^{obs,10}_{NONLIN}(2\pi\nu)||$ corresponding to the nonlinear dynamical responses obtained with four different load intensities f_0. The yellow band represents excitation frequency band $\mathbb{B}_e$. The upper left figure clearly shows a dynamical response which remains in the linear domain since there is numerically a negligible response contribution. On the other hand, subsequent contributions with unexpected resonances appear below and beyond excitation frequency band $\mathbb{B}_e$ for larger load intensities.

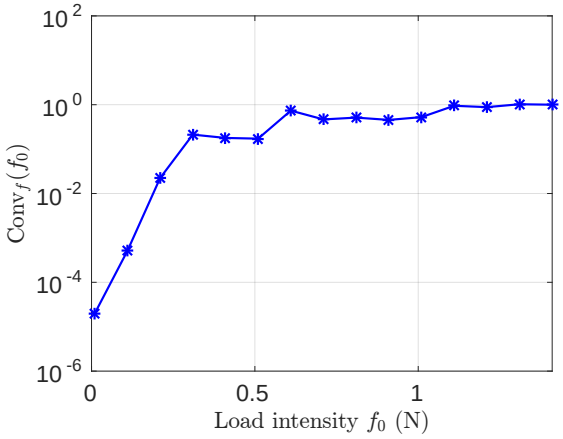

Figure 7: Sensitivity analysis with respect to the load intensity : graph of $f_0 \mapsto Conv_F(f_0)$.

3.5 Nonlinear dynamical response analysis

In this paragraph, a nonlinear dynamical analysis is performed for both tuned and detuned patterns $\mathcal{P}_1$ and $\mathcal{P}_2$. The time domain observation is chosen as $U_2^{obs,j_0}(t)$, which corresponds to the transverse dof expressed in the local frame related to observation node number j_0. The observation node is defined by

$$j_0 = \arg\left\{\max_j |||\mathbf{U}^{obs,j}|||\right\} \quad \text{with} \quad |||\mathbf{U}^{obs,j}||| = \max_t ||\mathbf{U}^{obs,j}(t)|| \quad , \tag{22}$$

in which $||\mathbf{U}^{obs,j}(t)||$ is defined similarly to Eq. (18). The frequency domain observation is then chosen as $||\widehat{\mathbf{U}}^{obs,j_0}(2\pi\nu)||$. The linear and the nonlinear analyses are presented with a load intensity $f_0 = 0.60\,N$ for both patterns $\mathcal{P}_1$ and $\mathcal{P}_2$, which correspond to moderate geometrical nonlinear effects. Figure 9 displays the graphs of $t \mapsto U^{obs,j_0}_{2,LIN}(t)$ for both patterns. It can be seen that both tuned and detuned structures yield different responses in the time domain. Figure10 displays the graphs of $t \mapsto U^{obs,j_0}_{2,NONLIN}(t)$ for both patterns. By comparing these figures, it can be seen that there are subsequent geometrical nonlinear effects. Furthermore, the observed nonlinear time response related to the considered detuned pattern $\mathcal{P}_2$ is clearly irregular, suggesting numerous resonances contributions outside $\mathbb{B}_e$. The nonlinear analysis is then carried out in the frequency domain by using a Fourier transform. Figure11 displays both graphs of $\nu \mapsto ||\widehat{\mathbf{U}}^{obs,j_0}_{LIN}(2\pi\nu)||$ and $\nu \mapsto ||\widehat{\mathbf{U}}^{obs,j_0}_{NONLIN}(2\pi\nu)||$ for both patterns. The main effect induced by the present detuning is to shift the

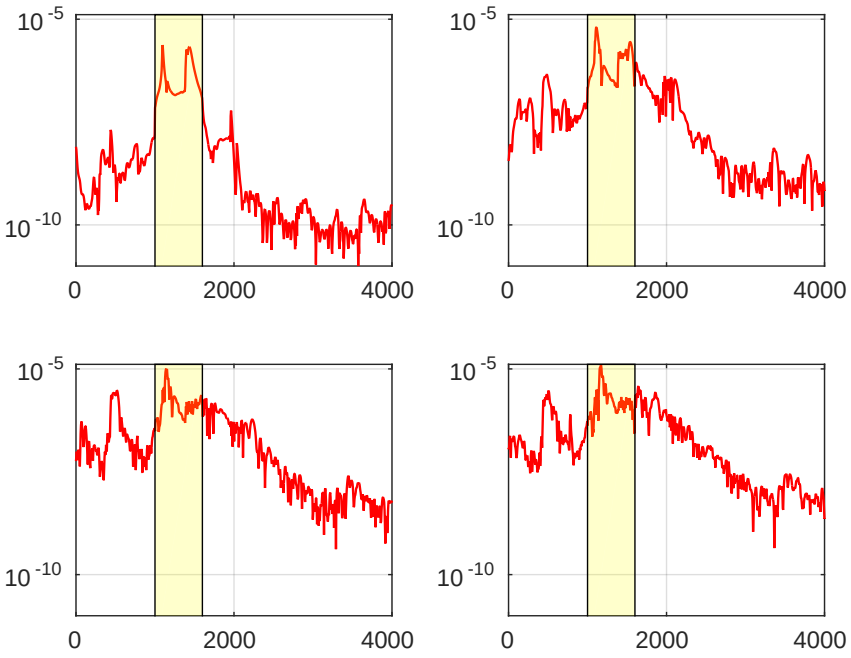

Figure 8: Sensitivity analysis with respect to the load intensity : representation of excitation frequency band $\mathbb{B}_e$ (light yellow zone), graphs of $\nu \mapsto ||\widehat{\mathbf{U}}^{obs,10}_{NONLIN}(2\pi\nu)||$ for $f_0 = 0.17\,N$ (upper left figure), $f_0 = 0.64\,N$ (upper right figure), $f_0 = 1.43\,N$ (lower left figure), $f_0 = 1.90\,N$ (lower right figure)

two main resonances related to the linear response to the left in the excitation frequency band. It is clearly observed that the geometrical nonlinear effects are stronger for the considered detuned pattern $\mathcal{P}_2$. For both patterns secondary resonances induced by the geometrical nonlinear effects appear below and above the excitation frequency band. This phenomenon is amplified for detuned pattern $\mathcal{P}_2$ and unexpected resonances with non negligible amplitudes exist for higher frequencies around $3\,000\,Hz$.

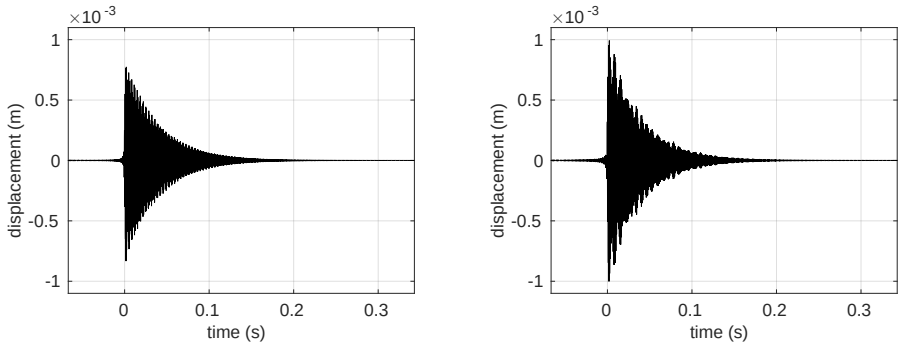

Figure 9: Linear dynamical analysis in the time domain: graphs of $t \mapsto U^{obs,j_0}_{2,LIN}(t)$ corresponding to patterns $\mathcal{P}_1$ (left figure) and $\mathcal{P}_2$ (right figure).

4 Conclusions

A methodology that allows the nonlinear dynamical analysis of rotating detuned structures is proposed in the context of geometrical nonlinearities. It should be noted that the nonlinear reduced-order model presented

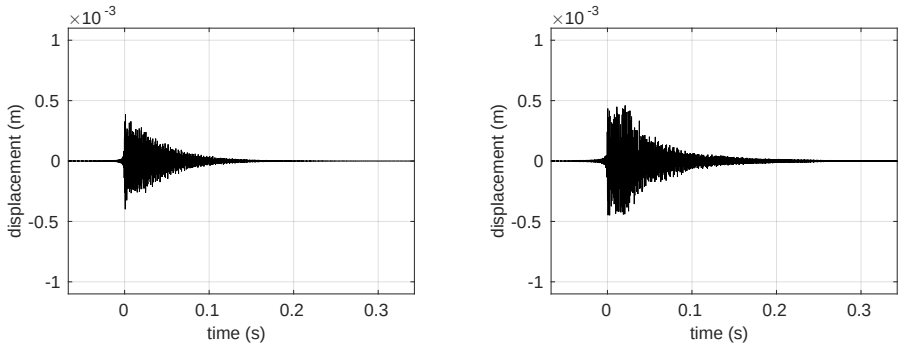

Figure 10: Nonlinear dynamical analysis in the time domain: graphs of $t \mapsto U^{obs,j_0}_{2,NONLIN}(t)$ corresponding to patterns $\mathcal{P}_1$ (left figure) and $\mathcal{P}_2$ (right figure).

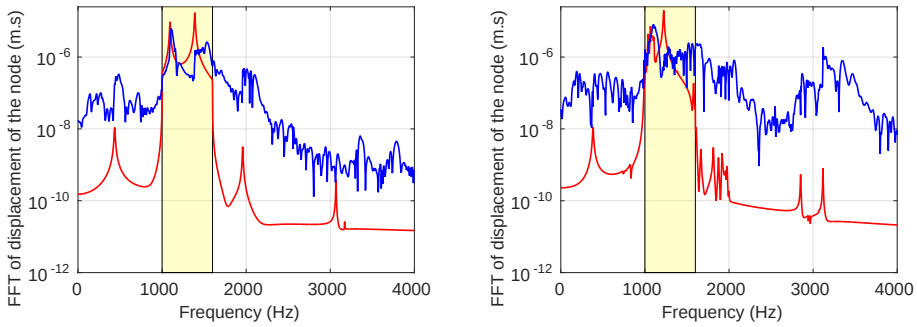

Figure 11: Nonlinear dynamical analysis in the frequency domain: graphs of $\nu \mapsto ||\widehat{\mathbf{U}}^{obs,j_0}_{LIN}(2\pi\nu)||$ (red line) and $\nu \mapsto ||\widehat{\mathbf{U}}^{obs,j_0}_{NONLIN}(2\pi\nu)||$ (blue line) corresponding to patterns $\mathcal{P}_1$ (left figure) and $\mathcal{P}_2$ (right figure).

in this work is also adapted for simultaneously modeling both detuning and mistuning.The results validate the numerical efficiency of the method and highlight the indirect excitation of the structure through the geometrical nonlinearities. Note that the numerical analysis is carried out on one tuned and one detuned pattern. The pattern optimization regarding the detuning is not considered in this work.

Acknowledgements

SafranTech is gratefully acknowledged for the permission to publish this work.

References

[1] D.J. Ewins. The effects of detuning upon the forced vibrations of bladed disks. *Journal of Sound and Vibration*, 9(1):65–79, 1969.

[2] D.S. Whitehead. The maximum factor by which forced vibration of blades can increase due to mistuning. *ASME Journal of Engineering for Gas Turbines and Power*, 120(1):115–119, 1998.

[3] M.P. Castanier, G. Ottarson, and C. Pierre. Reduced order modeling technique for mistuned bladed disks. *Journal of Vibration and Acoustics*, 119(3):439–447, 1997.

[4] M-T. Yang and J.H. Griffin. A reduced-order model of mistuning using a subset of nominal system modes. *ASME Journal of Engineering for Gas Turbines and Power*, 123(3):893–900, 2001.

[5] R. Bladh and M.P. Castanier. Component-mode-based reduced order modeling techniques for mistuned bladed disks-part 1: Theoretical models. *Journal of Engineering for Gas Turbines and Power*, 123(1):89–99, 2001.

[6] E. Capiez-Lernout, C. Soize, and M. Mbaye. Mistuning analysis and uncertainty quantification of an industrial bladed disk with geometrical nonlinearity. *Journal of Sound and Vibration*, 356:124–143, 2015.

[7] Aurelien Grolet and Fabrice Thouverez. Computing multiple periodic solutions of nonlinear vibration problems using the harmonic balance method and groebner bases. *Mechanical Systems and Signal Processing*, 52:529–547, 2015.

[8] C. Soize. A nonparametric model of random uncertainties for reduced matrix models in structural dynamics. *Probabilistic Engineering Mechanics*, 15(3):277–294, 2000.

[9] MP Mignolet and Christian Soize. Nonparametric stochastic modeling of linear systems with prescribed variance of several natural frequencies. *Probabilistic Engineering Mechanics*, 23(2-3):267–278, 2008.

[10] Matthew P Castanier and Christophe Pierre. Using intentional mistuning in the design of turbomachinery rotors. *AIAA journal*, 40(10):2077–2086, 2002.

[11] ByeongKeun Choi. Pattern optimization of intentional blade mistuning for the reduction of the forced response using genetic algorithm. *KSME international journal*, 17(7):966–977, 2003.

[12] M. Mbaye, C. Soize, J.-P. Ousty, and E. Capiez-Lernout. Robust analysis of design in vibration of turbomachines. *Journal of Turbomachinery*, 135(2):021008, 2013.

[13] C. Desceliers and C. Soize. Nonlinear viscoelastodynamic equations of three-dimensional rotating structures in finite displacement and finite element discretization. *International Journal of Nonlinear Mechanics*, 39:343–368, 2004.

[14] L. Sirovich. Turbulence and the dynamics of coherent structures. i. coherent structures. *Quarterly of applied mathematics*, 45(3):561–571, 1987.

[15] E. Capiez-Lernout, C. Soize, and M.-P. Mignolet. Computational stochastic statics of an uncertain curved structure with geometrical nonlinearity in three-dimensional elasticity. *Computational Mechanics*, 49(1):87–97, 2012.

[16] M.-P. Mignolet and C. Soize. Stochastic reduced order models for uncertain geometrically nonlinear dynamical systems. *Computer Methods in Applied Mechanics and Engineering*, 197(45-48):3951–3963, 2008.